ISTITUTO NAZIONALE DI FISICA NUCLEARE

Laboratori Nazionali di Frascati

PHASE CONTRAST IMAGING OPPORTUNITIES AT DAΦNE

Qiyue Hou[1,2] and A. Marcelli[1]

[1] *INFN-Laboratori Nazionali di Frascati Via E. Fermi 40, I-00044 Frascati, Italy*
[2] *NSRL, University of Science and Technology of China, 230029, Hefei, Anhui, P.R. China*

Abstract

This document is a feasibility study for a x-ray phase contrast imaging beamline using the emission of a DAΦNE wiggler. Taking in consideration source flux, coherence and geometrical parameters we compared the main x-ray phase contrast imaging methods: the Zernike phase contrast with a transmission X-ray microscopy (TXM), a X-ray coherent diffraction imaging (CDI), a diffraction enhanced imaging (DEI) and a X-ray Talbot interferometry (XTI). Considering the DAΦNE parameters, the Talbot-Lau interferometry appears the most suitable layout matching the wiggler source. We present and discuss the optical system of this beamline based on a spherical grating monochromator and two focusing mirrors.

INTRODUCTION

This document is a feasibility study of a beamline optical system dedicated to imaging matching the parameters of the DAΦNE wiggler source. The beamline is foreseen for multidisciplinary studies in materials science and life sciences. The synchrotron radiation source considered is one wiggler of the DAΦNE electron storage ring working at the nominal energy of 0.50 GeV. This device is a multi-pole electromagnet two meters long whose longitudinal magnetic field (applied in the vertical plane of the laboratory system) shown in Fig. 1. The flux produced by this wiggler device is reported in Fig. 2 for an accumulating current of 1000 mA and for the total horizontal divergence produced by this device (~180 mrad at 0.5 GeV). These values and the parameters of the wiggler determine a well-structured radiation source (see top view in Fig. 3) so that the radiation emitted by each pole can be easily identified. Electron beam emittances and sources size of the DAΦNE wiggler are listed in Table 1. [1]

PHASE CONTRAST IMAGING IN THE X-RAY REGION

Phase contrast imaging techniques in the X-ray region using a Transmission X-ray microscopy (TXM) are mainly based on the Zernike phase contrast technique. Other phase contrast techniques are based on the coherent X-ray diffraction microscopy, the diffraction enhanced imaging or the X-ray Talbot interferometry.

Zernike phase contrast with a TXM microscope
The setup of the Zernike phase contrast with a TXM is showed in Fig. 4. This layout doesn't need a coherent beam and its major requirement is to have the maximum incoherent flux. The overall optical layout of a TXM is similar to a visible light microscope [2]: the radiation is condensed before the sample and a magnified image is formed by an objective lens on the screen of a charge coupled device (CCD) detector. The two key optical elements of a TXM are the two lenses: the condenser and the zone plate objective. A zone plate is an optical element consisting of concentric zones with alternating optical refractive indexes that image the sample on the CCD. An elliptically shaped capillary can also be used as the condenser and, properly coupled with a beam stop and a pinhole aperture, it focuses a hollow central cone illumination to the sample and to the objective zone plate. The focusing efficiency of achievable capillary condensers is ~90%, significantly greater than a typical zone plate condenser (~10%) as those used in existing x-ray microscopes. In this layout a phase ring will be also added in the focal plane of the zone plate to take advantage of the Zernike phase contrast.

Coherent X-ray diffraction microscopy
The X-ray coherent diffractive imaging is a "lensless" technique that does not require high-quality lenses. On the contrary, compared to the Zernike phase contrast method, a

highly x-ray coherent beam is needed. The imaging system can work with a plane wave, a focused or a divergent beam. As an example, in Fig. 2 we show the coherent diffractive imaging setup available at the beamline ID01 at ESRF. [3] In this layout, a double-crystal Si(111) monochromator is set at 34 m from the source while the first pair of slits that defines the beam size are set at 38 m from the source (Fig. 5). Other two pairs of slits, set in front of the sample are used to spatially filter and clear out the beam. The first one of size 40(H)×40(V) μm^2 is located at 46 m from the source. The second pair is set 80 cm downstream and works as a guard slit to suppress the background scattering generated by the beam defining slits (see Fig. 5). Its size has to be adjusted during experiments to intercept the light scattered from the coherence defining slits having size of 100-120 μm, in both directions. If we consider the ID01 beamline parameters, the coherence length on the sample at the typical x-ray wavelengths, is few microns

$$\sigma_{\Delta x} \approx \frac{1}{2}\Delta_{\Delta x} = \frac{1}{2}\frac{l\lambda}{\Delta_x} = \frac{(47-46)m \times 0.155nm}{2*40\mu m} \approx 1.93\mu m \qquad (1)$$

a value slightly smaller or comparable to the typical sample dimensions (~5-10 μm).

Diffraction enhanced imaging
In the Diffraction Enhanced Imaging (DEI) a crystal analyzer allows detecting extremely subtle angular differences generated by the diffraction of the monochromatic radiation from the sample (see Fig.6). Due to interference effects, the intensity of the reflected spots of the diffraction pattern is highly dependent by the angle between the incident beam and the crystalline planes. When the incident angle is at the Bragg angle, monochromatic X-rays will remain in phase after reflection and, because of the constructive interference the reflected wave is characterized by a high intensity. Small changes in the angle of incidence (and reflection) may be achieved by a small rotation of the crystal. Moreover, at angles slightly above and below the Bragg angle, the intensity of the reflected beam described by its reflectivity curve, decreases rapidly. Actually, for a double crystal system, the reflectivity curve is the convolution of the reflectivity curves of the two crystals. To set at the maximum intensity the system, we have to optimize the angle and, to be succesfull, the angular resolution of the crystal rotation has to be ~0.1 μrad.

X-ray Talbot and Talbot-Lau interferometry
The X-ray Talbot Interferometry (XTI) schematically showed in Fig. 7(a) is based on two x-ray gratings. When a grating is illuminated by a coherent X-ray beam a phenomenon known as the Talbot effect occurs, i.e., periodic patterns (self-images) are generated at specific distances from the grating. If a sample is placed in front of the grating, depending by the differential phase shift induced by the sample, a deformation

of the self-image of the source is observed. In a XTI system, the deformation appears on the detector area as a Moiré pattern because of the contribution of the second grating, i.e., the amplitude grating located at the self-image position. The differential phase shift induced by the sample can be quantitatively retrieved by a fringe scanning technique, which is performed with a translation of one of the two gratings in the direction of its period. [4,5] As showed in Fig. 7(b), if the spatial coherence of the X-ray beam is not sufficient to generate an X-ray phase contrast, a third grating G0 near the X-ray source has to be introduced. If a single slit source illuminates the Talbot interferometer, i.e., the G1 and G2 gratings, a Moire' pattern behind G2 can be observed. Therefore, the period of the first grating has to be chosen in order that Moire' patterns generated by all slits coincide and simultaneously compose. The optical configuration showed in Fig. 7(b) is also recognized as a Talbot–Lau interferometer.

THE DAΦNE BEAMLINE AND THE OPTICAL SYSTEM

Considering both flux and source sizes, the performance of the DAΦNE wiggler is higher than the DAΦNE bending magnets by a factor ~30 (60 times is for the higher flux while it reduces ~1/2 because of size). However, for soft x-ray applications the x-ray DAΦNE wiggler source is better then a bending magnet source of the same ring because a monochromator system is more sensible to the vertical size of the source. The parameters of the imaginary Gaussian source located in the wiggler center are summarized in Table 2. Its FWHM can be calculated as:

$$FWHM = 2\sqrt{2\ln 2}\,\sigma \qquad\qquad (2)$$

Different beamline optical layouts have been considered and a spherical grating monochromator (SGM) with two focusing mirrors or a single toroidal mirror have been considered as the most suitable configuration. Because a single toroidal mirror can be more complex to fabricate with low aberrations, an optical system with a grating and two spherical mirrors is preferable.

In more detail two setups can be considered: a SGM with a Horizontal and a Vertical Focusing Mirrors (HFM&VFM), and a Dragon-like system [7]. The first layout utilizes two mirrors to focus the beam to the entrance slit in both directions while beam is then monochromatized and re-focused vertically by a cylindrical grating. The vertical secondary source is then located at the position of the exit slit of the optical system. Its position shifts with the energy while the horizontal one remains fixed at the entrance slit. Unlike the first layout, the HFM in the Dragon-like system focus the beam at the "sample position", but actually using data of the Ref. 7, the beam is actually focused at 0.624 m before the entrance slit, where the beam width has the smallest size. The vertical radiation is focused at the entrance slit of the monochromator by the VFM, then the cylindrical grating monochromator focus the radiation to the fixed exit slit. In the next we will define the exit slit of both monochromators as the Plane 0. Parameters of

the secondary virtual source such as position, size, angular divergence and photon flux are summarized in Table 3. Starting by the Lagrange-Helmholtz invariants:

$$\sigma'_{x_s} = \frac{\sigma_x \sigma'_x}{\sigma_{x_s}} = \frac{0.79cm \times 2.13mrad}{FWHM_{x_s} / 2\sqrt{2\ln 2}} \qquad (3)$$

$$\sigma'_{z_s} = \frac{\sigma_z \sigma'_z}{\sigma_{z_s}} = \frac{0.015cm \times 0.36mrad}{FWHM_{z_s} / 2\sqrt{2\ln 2}} \qquad (4)$$

or combining Eq.s (11) and (14) with the Eq.(9) after a free propagation, the divergence angles can be calculated.

PHASE CONTRAST IMAGING AT DAΦNE

Zernike phase contrast with a TXM

In this method, we select the exit slit plane for both conditions as the front focus of the ellipsoidal condenser. The fraction of the light that meets the accepted divergence of the condenser illuminates the sample. From Table 3, we can see that for the HFM &VFM condition, the lateral size of the beam image of the condenser is 1000 times larger than the vertical size, while for the Dragon-like system, the difference in size is only 20 times larger. In addition, the semi-minor axis of the ellipsoidal condenser should be larger than the source size at the focus, which is 10.4 cm for the HFM & VFM layout and 4.3 cm for the Dragon-like system. In this case, in order to accept radiation with a vertical divergence of ~1 *mrad* for the HFM&VFM layout, and a horizontal divergence of ~3 *mrad* for the Dragon-like system, the distance between the two focuses should be at least 104 m or 14 m, actually too large to fit the available space. Finally, the horizontal secondary source for both conditions are never at the focus of the condenser, thus the center of the source will be lost at the image plane of the condenser. Therefore, these conditions are not compatible with a Zernike phase-contrast imaging layout.

Coherent X-ray diffraction microscopy

Considering x-ray diffraction imaging we need a coherent radiation beam. The coherence angles of the imaginary source of the DAΦNE wiggler may be obtained by the width-angle product in the two directions:

$$\sigma'_{\Delta x} = \frac{\lambda}{4\pi} \frac{1}{\sigma_x} \approx \frac{1nm}{4\pi} \frac{1}{0.79cm} \approx 1.0 \times 10^{-8} rad \qquad (5)$$

$$\sigma'_{\Delta z} = \frac{\lambda}{4\pi} \frac{1}{\sigma_z} \approx \frac{1nm}{4\pi} \frac{1}{0.015cm} \approx 5.29 \times 10^{-7} rad \qquad (6)$$

To fulfill the coherent radiation conditions and collect a coherent flux from this source

with these extremely small angles we need a slit selecting just a few μrad in the vertical direction and a few *nrad* in the horizontal direction. These settings significantly reduce the flux

$$\frac{\sigma'_{\Delta x} \sigma'_{\Delta z}}{\sigma'_x \sigma'_z} \approx 7 \times 10^{-9} \qquad (7)$$

In principle, there are many advantages using a CDI technique. As an example, in-vacuum x-ray diffraction microscopy minimizes unavoidable contributions due to sample motions. Moreover, the windowless vacuum environment of CDI may also minimize the background scattering, and, reconstruction of 3D structural information on the Ewald sphere can be obtained from a single view. However, because all CDI applications need a large coherent flux ($\sim 10^9 - 10^{12} \, photons / s / 0.1 BW$) or an X-ray laser source, the Eq. 7 points out that the flux available from the DAΦNE wiggler is not suitable for any X-ray diffraction imaging applications

Diffraction enhanced imaging
The DEI method is a method based on a crystal monochromator coupled to a perfect crystal measuring the refractive angle. However, suitable crystal monochromators are not available for the energy of the DAΦNE wiggler ($\varepsilon_c \sim 300$ eV) and a grating monochromator is the only option at these wavelengths. As a consequence diffraction enhanced imaging methods are complex and expensive to be implemented.

X-ray Talbot interferometry
In a Talbot interferometry imaging system we have two gratings G1, and G2 with periods T_1, T_2, respectively. For the DAΦNE case, source sizes and divergence angles on the vertical or horizontal secondary source planes are listed in Table 3. After the grating monochromator, the beam is quasi monochromatic, and its mutual intensity distribution on the vertical direction at the vertical secondary source is independent by time. It can be written as:

$$J_V \left(z_s + \frac{\Delta z_s}{2}, z_s - \frac{\Delta z_s}{2} \right) \propto \exp\left(-\frac{z_s^2}{2\sigma_{z_s}^2} \right) \exp\left(-\frac{(\Delta z_s)^2}{2\sigma_{\Delta z_s}^2} \right) \qquad (8)$$

$$\sigma_{\Delta z_s} = \frac{\lambda}{2\pi \sigma'_{z_s}} \qquad (9)$$

where $\sigma_{z_s}^2$ and $\sigma_{\Delta z_s}^2$ refer to the width of the beam and to the coherence width on the vertical direction, respectively. The subscript z_s is the vertical secondary source plane. According to the propagation of the mutual intensity in the free space, the mutual intensity on the vertical direction can be written as:

$$J_1\left(z_1+\frac{\Delta z_1}{2}, z_1-\frac{\Delta z_1}{2}\right)$$

$$=\frac{e^{j\theta}}{\left(\lambda l_{s_v 1}\right)^2}\iint J_V\left(z_s+\frac{\Delta z_s}{2}, z_s-\frac{\Delta z_s}{2}\right)\exp\left(j\frac{2\pi}{\lambda l_{s_v 1}}\left[\left(z_s+\frac{\Delta z_s}{2}\right)^2-\left(z_s-\frac{\Delta z_s}{2}\right)^2\right]\right)$$

$$*\exp\left(-j\frac{2\pi}{\lambda l_{s_v 1}}\left[\left(z_1+\frac{\Delta z_1}{2}\right)\left(z_s+\frac{\Delta z_s}{2}\right)-\left(z_1-\frac{\Delta z_1}{2}\right)\left(z_s-\frac{\Delta z_s}{2}\right)\right]\right)dz_s d\Delta z_s \qquad (10)$$

$$=\frac{e^{j\theta}}{\left(\lambda l_{s_v 1}\right)^2}\iint J_V\left(z_s+\frac{\Delta z_s}{2}, z_s-\frac{\Delta z_s}{2}\right)\exp\left(j\frac{2\pi}{\lambda l_{s_v 1}}z_s\Delta z_s\right)\exp\left(j\frac{2\pi}{\lambda l_{s_v 1}}(\Delta z_1 z_s+\Delta z_s z_1)\right)z_s d\Delta z_s$$

$$\propto e^{j\theta}\exp\left(-\frac{z_1^2}{2\sigma_{z1}^2}\right)\exp\left(-\frac{(\Delta z_1)^2}{2\sigma_{\Delta z1}^2}\right)$$

where

$$\sigma_{z1}^2=\left(\frac{\lambda l_{s_v 1}}{2\pi\sigma_{\Delta z_s}}\right)^2+\sigma_{z_s}^2$$

$$(11)$$

$$\sigma_{\Delta z1}^2=\left(\frac{\lambda l_{s_v 1}}{2\pi\sigma_{z_s}}\right)^2+\sigma_{\Delta z_s}^2$$

and

$$\theta=\frac{k}{l_{s_v 1}}z_1\Delta z_1 \qquad (12)$$

with σ_{z1} and $\sigma_{\Delta z1}$ are the beam and the coherence width, respectively, on the plane of G1. Similarly, the mutual intensity on the horizontal direction can be written as:

$$J_1\left(x_1+\frac{\Delta x_1}{2}, x_1-\frac{\Delta x_1}{2}\right)\propto e^{j\theta}\exp\left(-\frac{x_1^2}{2\sigma_{x1}^2}\right)\exp\left(-\frac{(\Delta x_1)^2}{2\sigma_{\Delta x1}^2}\right) \qquad (13)$$

where

$$\sigma_{x1}^2=\left(\frac{\lambda l_{s_h 1}}{2\pi\sigma_{\Delta x_s}}\right)^2+\sigma_{x_s}^2$$

$$(14)$$

$$\sigma_{\Delta x1}^2=\left(\frac{\lambda l_{s_h 1}}{2\pi\sigma_{x_s}}\right)^2+\sigma_{\Delta x_s}^2$$

and

$$\theta=\frac{k}{l_{s_h 1}}x_1\Delta x_1 \qquad (15)$$

Here σ_{xs}^2 refers to the width of the beam, $\sigma_{\Delta xs}^2$ refers to the coherence width on the horizontal direction, the subscript x_s represents the horizontal secondary source plane and $l_{s_h 1}, l_{s_v 1}$ are the distances from the horizontal or vertical secondary source to the

grating G1, respectively. Using the parameters on the secondary source plane, we obtained on the plane of G1 the parameters listed in Table 4, at 2 m from the 0 plane. From the self-intensity in Eq.(18), when the coherence width fulfill the condition:

$$\sigma_{\Delta z1}\left(\sigma_{\Delta x1}\right) \geq pT_1; \; p = \frac{1}{2}, \frac{3}{2}, \dots \tag{16}$$

the first order of self-image does not vanish. From the above we can see that the coherence width should at least larger than half of the period of G1. Considering the coherence widths on the G1 plane and the period of the grating G1 (5 μm) both conditions in the vertical direction are compatible with a Talbot interferometer. From the Eq. (16), p can have a semi-integer value: 1/2 or 3/2 for the HFM&VFM layout and 1/2 for the Dragon-like system.

In the X-ray Talbot interferometer, the grating G1 is always a phase grating. In particular, due to the limited space available, we choose a $\pi / 2$ phase grating located at 2 m from the 0 plane. In the soft-X-ray region, a phase grating with a period ~5 μm is available. The grating G2 (i.e., the absorption grating) can be placed at:

$$l_{12} = p\frac{T_1^2}{\lambda}\frac{R_{v1}}{R_{v1} - p\left(T_1^2 / \lambda\right)}, \; p = \frac{1}{2}, \frac{3}{2}, \dots \tag{17}$$

where R_{v1} is the curvature radius on the grating G1 along the vertical direction. It can be calculated as

$$R_{v1} = l_{s_v 1}\left(\frac{k^2 \sigma_{z_s}^2 \sigma_{\Delta z_s}^2}{l_{s_v 1}^2} + 1\right) \tag{18}$$

and its self- image can be written as:

$$I_{self} = I_0 \frac{\sigma_{x2}}{\sigma_{x1}}\frac{R_{v1}}{\left(R_{v1} + l_{12}\right)}\sum_n \mu_n b_n \exp\left(2\pi i \frac{n}{T_2} z\right) \tag{19}$$

where I_0 is the intensity before the grating G1 and μ_n is the complex coherence factor:

$$\mu_n = \mu\left(np T_1\right) = \exp\left(-\frac{\left(np T_1\right)^2}{2\sigma_{\Delta z_1}^2}\right) \tag{20}$$

The b_n is the nth Fourier coefficient of the intensity pattern required by a completely coherent illumination

$$b_n = \sum_{n'} a_{n'+n} a_{n'}^* \exp\left[-i\pi p\left(\left(n' + n\right)^2 - n'^2\right)\right] \tag{21}$$

and I_0 and T_2 are:

$$I_0 = \frac{flux}{FWHM_{x_1} \times FWHM_{z_1}} \tag{22}$$

$$T_2 = \frac{R_{v1} + l_{12}}{R_{v1}} T_1 \tag{23}$$

where a_n is the nth Fourier coefficient of the complex transmission of the second grating. From the Eq.(23), we know that the differential phase signal is proportional to the distance between G1 and G2, and p has a negligible effect on the q1 and q0 factors. In addition, since the distance is much smaller than $l_{z\,max}$, where the Talbot effect disappears as described in Eq. (24), p has not to be too small and the influence on the field of view is negligible:

$$l_{12} \ll l_{z\,max} = \frac{R_{v1} + l_{12}}{R_{v1}} \frac{FWHM_{z_1} T_1}{\lambda} \tag{24}$$

All considered, we chosen for p the value of 3/2 for the HFM&VFM layout and of 1/2 for the Dragon-like system. All parameters of the Talbot interferometer are summarized in Table 5.

X-ray Talbot-Lau interferometer

Although the phase signal is proportional to the self-image distance, in a Talbot interferometer the distance is rather small due to the limited coherence width on the plane G1 and the need to add the absorbing grating G2. Therefore, to work with a relatively large self-image distance we have to consider a Talbot-Lau interferometer with another grating G0 on the Plane 0. Although this layout fits a low coherence width on the Plane 0, from the table 4 we select the vertical direction to set G0 on the vertical secondary sources. If we consider the single slit source of width a splits by G0, the horizontal position is z_a, and after the exit slit of the monochromator the complex amplitude function is $t(z_0)$. The mutual intensity can be written as:

$$J_0'\left(z_0 + \frac{\Delta z_0}{2}, z_0 - \frac{\Delta z_0}{2}\right) = J_0\left(z_0 + \frac{\Delta z_0}{2}, z_0 - \frac{\Delta z_0}{2}\right) t\left(z_0 + \frac{\Delta z_0}{2}\right) t^*\left(z_0 - \frac{\Delta z_0}{2}\right)$$

$$\propto \exp\left(-\frac{z_0^2}{2\sigma_{z_0}^2}\right) \exp\left(-\frac{(\Delta z_0)^2}{2\sigma_{\Delta z_0}^2}\right) rect\left(\frac{z_0 - z_a}{a - |\Delta z_0|}\right) \tag{25}$$

From the term

$$\exp\left(-\frac{(\Delta z_0)^2}{2\sigma_{\Delta z_0}^2}\right)$$

in the Eq.(25), we know that $\left|\Delta z_0\right| \le 2\sigma_{\Delta z_0}$. If $2\sigma_{\Delta z_0} \ll a$ and $a \ll \sqrt{2\pi}\sigma_{z_0}$, the above formula can be simplified as:

$$J_0'\left(z_0+\frac{\Delta z_0}{2}, z_0-\frac{\Delta z_0}{2}\right) \propto \exp\left(-\frac{z_0^2}{2\sigma_{z_0}^2}\right)\exp\left(-\frac{\left(\Delta z_0\right)^2}{2\sigma_{\Delta z_0}^2}\right)rect\left(\frac{z_0-z_a}{a\left(1-\left|\Delta z_0\right|/a\right)}\right)$$
$$\approx \exp\left(-\frac{z_a^2}{2\sigma_{z_0}^2}\right)\exp\left(-\frac{\left(\Delta z_0\right)^2}{2\sigma_{\Delta z_0}^2}\right)rect\left(\frac{z_0-z_a}{a}\right) \quad (26)$$

We may also reshape the rectangle of width a and unitary height with a Gaussian with the same area as in the Eq.(27) with a RMS width $a/\sqrt{2\pi}$ and again unitary height:

$$rect\left(\frac{z_0-z_a}{a}\right) \approx \exp\left(-\pi\frac{\left(z_0-z_a\right)^2}{a^2}\right) \quad (27)$$

therefore, the beam width and the coherence width on the plane of G1 of the mutual intensity described by Eq.(11), become:

$$\sigma_{z_1}^2 = \left(\frac{\lambda l_{01}}{2\pi\sigma_{\Delta z_0}}\right)^2 + \left(\frac{a}{\sqrt{2\pi}}\right)^2$$
$$\sigma_{\Delta z_1}^2 = \left(\frac{\lambda l_{01}}{\sqrt{2\pi}a}\right)^2 + \sigma_{\Delta z_0}^2 \quad (28)$$

where l_{01} is the distance from the 0 plane to the grating G1. Combining the above widths with the Eq.(16), we obtain

$$a \le \frac{\lambda l_{01}}{\sqrt{2\pi\left[\left(pT_1\right)^2 - \sigma_{\Delta z_0}^2\right]}} \approx \frac{160\mu m}{p} \quad (29)$$

and the period of the grating G0 is

$$T_0 = R_{v1} \times T_2 / l_{12} \quad (30)$$

where l_{12} is the self-distance. If the equality in Eq.(29) is fulfilled, the parameter p has the same effect on both factors q1 and q0. In this set-up, considering the $l_{z\max}$ described in the Eq.(24) and the practical limitations on opening and non-opening sizes in the grating manufacture ($\sim \mu m$), p can reach the value of 38.5 for the HFM &VFM system, or 49.5 for the Dragon-like system. However, due to the limited space we set p to 15.5 for both conditions. The corresponding source sizes on the grating G1 are:

$$W_{x_1} = 2\sqrt{2\ln 2}\,\sigma_{x_1}$$
$$W_{z_1} \approx 2\sqrt{2\ln 2}\,\sigma_{z_1} + FWHM_{z_0} \qquad (31)$$

and in the Talbot-Lau interferometer, the self-image due to a split beam can also be written as Eq.(18), where I_0 is the intensity before the grating G1:

$$I_0 = \frac{f\,lux}{W_{x1} * W_{z1}} \qquad (32)$$

All parameters of this configuration are summarized in Table 6.

Comparison of the Talbot and Talbot-Lau interferometers
In a Talbot-Lau interferometer with a third grating whose n^{th} Fourier coefficient of the intensity transmission function is c_n, if we set the ideal value of $c_1 / \sqrt{c_0} = 0.48$ [6], inclined by θ respect to the second grating, the intensity I of the Moiré pattern is:

$$I = I_0 \sum_n \frac{R_{v1}}{(R_{v1}+l_{12})} \frac{\sigma_{x_1}}{\sigma_{x_2}} T_s \mu_n b_n c_n \exp\left\{2\pi i \frac{n}{T_2}\left(-z\theta + l_{12}\varphi_{z_s}\right)\right\} \qquad (33)$$

where z_s is the coordinate of the sample, T_s is the transmission and Φ is the phase shift of the sample and the expression of φ_{z_s} is

$$\varphi_{z_s} = \frac{\lambda}{2\pi}\frac{\partial \Phi}{\partial z_s} \qquad (34)$$

If we define q_n as

$$q_n = \frac{R_{v1}}{(R_{v1}+l_{12})} \frac{\sigma_{x_1}}{\sigma_{x_2}} \mu_n b_n c_n T_s \qquad (35)$$

similar formulas can be derived for a Talbot interferometer. If the error is negligible when compared to the signal, we may also write [6]

$$\Delta\varphi = \frac{T_2}{2\pi l_{12}} \frac{\sqrt{q_0}}{q_1} \frac{1}{\sqrt{2}} \frac{1}{\sqrt{I_0 t_{total}\Delta^2}} \qquad (36)$$

If we select a sample made by a polypropylene ellipsoid of diameter D=5 cm and thickness t=8 μm immersed in a 10 μm thick water and sets it before the grating, assuming a $1/e^2$ transmission behavior, at the energy of ~1 keV the x-ray penetration of an equivalent water thickness (i.e., the background) is ~10 μm. The maximum signal is:

$$\varphi_{\max} = 2\frac{t}{D}\sqrt{\frac{D}{(l_{01}+l_{12})/l_{01}\Delta}}(\Delta\delta) \tag{37}$$

where $\Delta\delta$ is the difference among the refractive index between polypropylene and water and Δ is the pixel size. Actually, if the SNR is $> 5\sim10$, the signal of the differential phase shift that can be detected is

$$SNR = \frac{\varphi_{\max}}{\Delta\varphi} = 5\sim10 \tag{38}$$

The spatial resolution of a Talbot or a Talbot-Lau interferometer is

$$\Delta_{res_h} = \frac{\sigma_{x_1}}{\sigma_{x_2}}\Delta, \Delta_{res_v} = \frac{R_{v1}\Delta}{R_{v1}+l_{12}} \tag{39}$$

where Δ_{res_h} and Δ_{res_v} are the horizontal and vertical resolution, respectively. Because the source is smaller than the sample, we need scanning the sample area. Assuming the SNR at the edge > 10, the calculate photon numbers within one pixel, the dose released to the sample and the total time including the raster scans are listed in Table 7. From these values, we may point out that although a Talbot-Lau interferometer needs an additional source grating, its performances are better than a Talbot interferometer. Indeed, both the dose and the total acquisition time are smaller by $1\sim2$ orders of magnitude due to its larger phase signal. Also the spatial resolution on the vertical direction is improved due to the larger self-distance. If we compare the HFM&VFM and the Dragon-like layouts, because of its lower dose and reduced time the HFM&VFM system matches better a Talbot-interferometer, while a Talbot-Lau interferometer is more suitable for a Dragon-like system due the lower number of scans. For what concern the resolution, it mainly depends by the pixel size of the detector. If a sub-micron resolution is desired, the differential phase X-ray imaging microscopy with an X-ray Talbot interferometer is nice [8], because it may add a focusing element such as a X-ray zone plate in front of the grating.

Stability of the source
To evaluate the requirement of the source stability for both optical configurations, we considered the stability of beam direction, beam position and beam divergence. For what concern beam position and divergence, to maintain the beam in focus and minimize effects on the detector a stability of 10% of the beam size has to be considered. Therefore, the stability of the beam position or of the beam divergence of the imaginary source are 0.79 mm and 0.213 mrad in the horizontal direction, and 0.05 mm and 0.036 mrad in the vertical direction, respectively. Considering the stability of the beam direction, we have to consider the contribution of the monochromator and the

mutual intensity on the grating G1. The diffraction equation of a grating monochromator is:

$$d\left(\sin\alpha + \sin\beta\right) = m\lambda \qquad (40)$$

where α is the incident angle, β is the diffraction angle, m is the diffraction order, and d is the period of the cylindrical grating. From the Eq.(40), we can see that the shift of the selected wavelength $\delta\lambda$ will change with the shift of the incident angle $\delta\alpha$:

$$\delta\lambda = d\cos\alpha\,\delta\alpha \qquad (41)$$

and, if the spectral resolution is $\Delta\lambda/\lambda = 10^{-3}$ the shift of the selected wavelength has to be smaller than $\Delta\lambda$ to have:

$$\delta\alpha \le \frac{10^{-3}\lambda}{d\cos\alpha} \qquad (42)$$

Working with a 1200 lines/cm cylindrical grating, in the HFM&VFM optical system with an incident angle of 88° and with 89.11° in the Dragon-like system, the stability of the beam direction of these optical systems are given in Table 8. As can be seen in Fig.(8), when the beam direction changes, according to the diffraction of mutual intensity described in Eq.(39) the mutual coherence function on the grating G1 is

$$J_1' = \int\int J_0' \frac{\exp\left[j\overline{k}\left(r_1 - r_2\right)\right]}{\overline{\lambda}^2 r_1 r_2} dO_1 dO_2 \qquad (43)$$

where r_1, r_2 is the distances $P_1'O_1, P_2'O_2$. Here we defined the x-z plane of the coordinate system parallel to the grating G1, so that the mutual intensity of the secondary source is:

$$J_0' = J_0\left(\frac{x_0}{\cos\delta}, z_0; \frac{x_0'}{\cos\delta}, z_0'\right) \qquad (44)$$

where J_0 is the mutual intensity before the change of the direction. If the latter changes in the vertical direction ($\delta\alpha$), within the paraxial approximations the distances r_1, r_2 can be written as:

$$r_1 = \sqrt{\left(x_1 - x_0\right)^2 + \left(z_1 - z_0\right)^2 + \left(l_{01} + x_0\tan\delta\right)^2}$$

$$\approx l_{01} + \frac{1}{2l_{01}}\left(x_1^2 + z_1^2\right) + \frac{1}{2l_{01}}\left[z_0^2 + \left(\frac{x_0}{\cos\delta}\right)^2 - 2z_1z_0 - 2\left(x_1 - l_{01}\tan\delta\right)x_0\right]$$

$$r_2 = \sqrt{\left(x_1' - x_0'\right)^2 + \left(z_1' - z_0'\right)^2 + \left(l_{01} + x_0'\tan\delta\right)^2} \qquad (45)$$

$$\approx l_{01} + \frac{1}{2l_{01}}\left(x_1'^2 + z_1'^2\right) + \frac{1}{2l_{01}}\left[z_0'^2 + \left(\frac{x_0'}{\cos\delta}\right)^2 - 2z_1'z_0' - 2\left(x_1' - l_{01}\tan\delta\right)x_0'\right]$$

therefore, the mutual intensity is given by the following equation when $t_0 = x_0 / \cos\delta$:

$$J_1^{'} = \frac{\exp(j\theta)}{\bar{\lambda}^2 l_{01}^2} \iiint J_0\left(t_0, z_0, t_0^{'}, z_0^{'}\right) \exp\left\{\frac{jk}{2l_{01}}\left[\left(t_0^2 + z_0^2\right) - \left(t_0^{'2} + z_0^{'2}\right)\right]\right\}$$

$$\exp\left\{-\frac{jk}{l_{01}}\left[z_1 z_0 + \left(x_1 \cos\delta - l_{01}\sin\delta\right)t_0 - z_1^{'} z_0^{'} - \left(x_1^{'}\cos\delta - l_{01}\sin\delta\right)t_0^{'}\right]\right\} dz_0 dz_0^{'} dt_0 dt_0^{'} \quad (46)$$

$$\theta = \frac{k}{2l_{01}}\left[\left(x_1^2 + z_1^2\right) - \left(x_1^{'2} + z_1^{'2}\right)\right]$$

and when combined with the diffraction of the mutual intensity before a change of the direction:

$$J_1 = \frac{\exp(j\theta)}{\bar{\lambda}^2 l_{01}^2} \iiint J_0\left(x_0, z_0, x_0^{'}, z_0^{'}\right) \exp\left\{\frac{jk}{2l_{01}}\left[\left(x_0^2 + z_0^2\right) - \left(x_0^{'2} + z_0^{'2}\right)\right]\right\}$$

$$\exp\left\{-\frac{jk}{l_{01}}\left[x_1 x_0 + z_1 z_0 - x_1^{'} x_0^{'} - z_1^{'} z_0^{'}\right]\right\} dx_0 dx_0^{'} dz_0 dz_0^{'} \quad (47)$$

we obtain the mutual intensity:

$$J_1^{'} = J_1\left(x_1 \cos\delta - l_{01}\sin\delta, z_1, x_1^{'}\cos\delta - l_{01}\sin\delta, z_1^{'}\right) \quad (48)$$

From the above equation we may see that the mutual intensity displacement is $l_{01}\tan\delta$ that increases as $1/\cos\delta$. If the total change has to be $< 10\%$, it requires that:

$$\left|\frac{FWHM_{x1}}{2}\cos\delta - l_{01}\sin\delta - \frac{FWHM_{x1}}{2}\right| \leq 10\% FWHM_{x1} \quad (49)$$

and

$$\left|\frac{FWHM_{z1}}{2}\cos\delta - l_{s_v1}\sin\delta - \frac{FWHM_{z1}}{2}\right| \leq 10\% FWHM_{z1} \quad (50)$$

CONCLUSION

Considering the source flux, the coherence and the geometrical parameters of the DAΦNE wiggler and the different x-ray phase contrast imaging methods, this study suggests the Talbot-Lau interferometry as the most suitable layout to match the structured wiggler source of DAΦNE. The Talbot-Lau interferometry measures the differential phase shift, and it is very sensitive to edges and interfaces and can be used to observe small details inside a sample. Moreover, if we consider the soft x-ray range

(1~2 keV) at energies well above the water window the phase contrast has to be preferred to the absorption contrast. Actually, the Talbot-Lau is a very powerful method to image soft biological samples with a high contrast. In addition, its field of view is quite large, from mm up to cm allowing imaging of soft samples with thickness of ~10 μm. We also presented and discussed the relative advantages of two possible optical systems based on a spherical grating monochromator and two focusing mirrors.

ACKNOWLEDGEMENTS

REFERENCES

(1)   A. Marcelli and P. Calvani, Internal Report LNF-93/027 (IR) 14 June 1993
(2)   Y.C. Tian *et al*., Rev. Sci. Instrum. **79**, 103708 (2008)
(3)   A. Schropp *et al*., IPAP Conf. Series 7, 383-385 (2006)
(4)   A. Momose *et al*., Japanese Journal of Applied Physics **45**, 6A (2006)
(5)   A. Momose *et al*., Japanese Journal of Applied Physics **48**, 076512 (2009)
(6)   W. Yashiro *et al*., J. Opt. Soc. Am. A **25**, 8 (2008)
(7)   M. Sanchez del Rio and A. Marcelli, *Ray tracing of a soft x-ray beamline for DAΦNE wiggler* (*private commun*.)
(8)   T. Yoshihiro et al., Appl. Phys. Express **1** 117002 (2008)
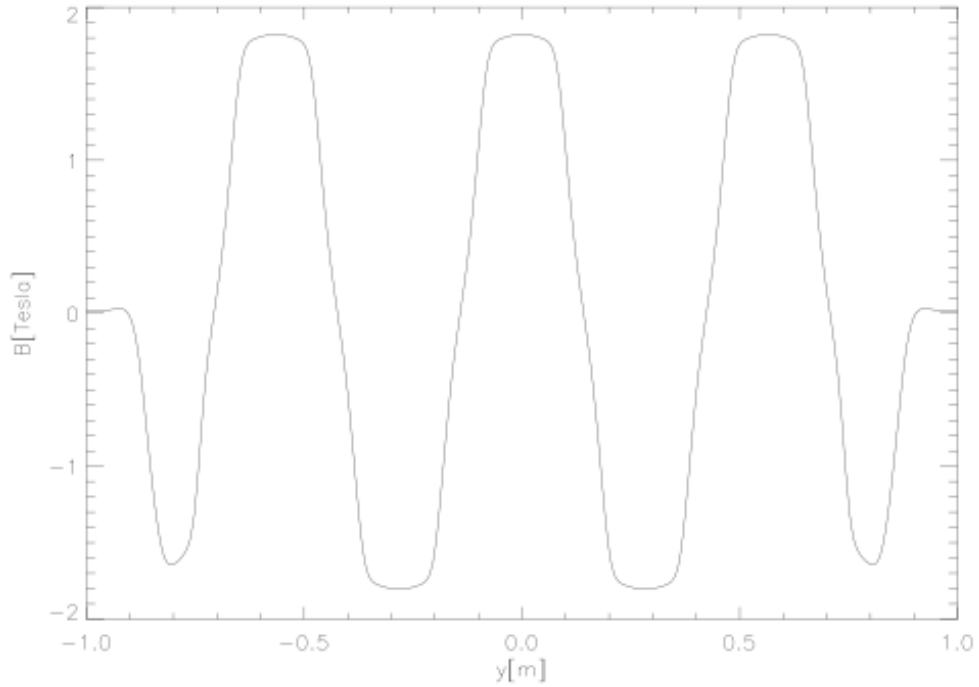
Figures and tables

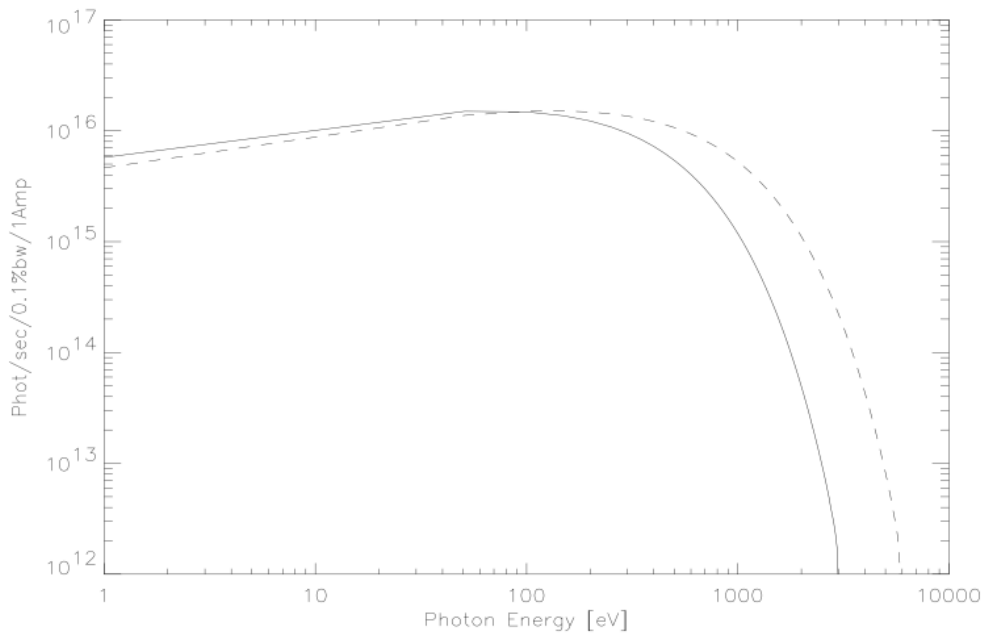**FIG. 1** The magnetic field of the DAΦNE wiggler along the longitudinal axis.

FIG. 2 Photon flux spectra of the DAΦNE wiggler at the electron energy of 0.5 GeV (line) and 0.7 GeV (dotted line).
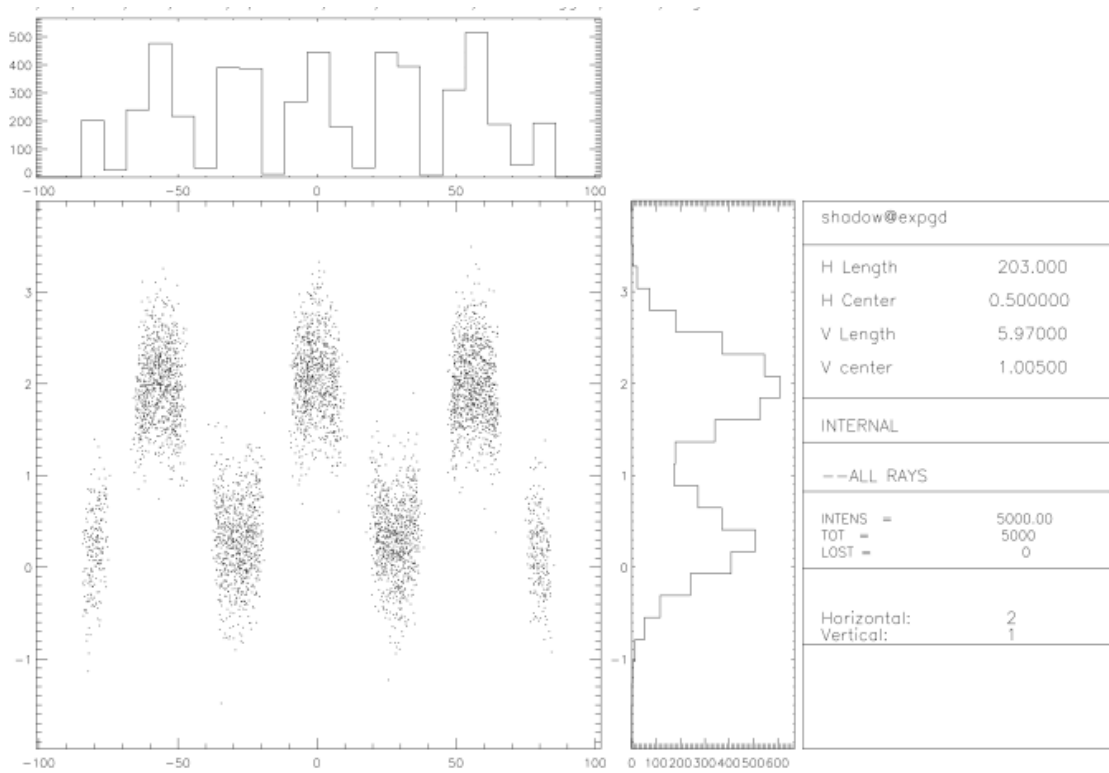
FIG. 3 Top view of the radiation emission of the DAΦNE wiggler at 0.5 GeV and at the photon energy of 1.5 keV.
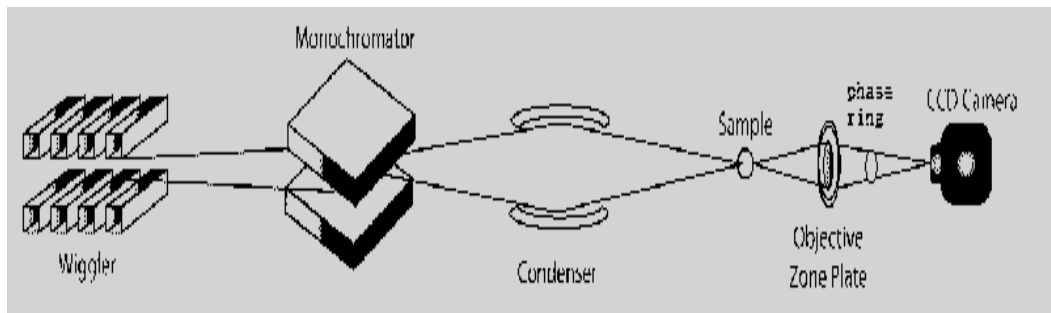

FIG. 4: Optical layout of a Zernike phase contrast imaging microscope.
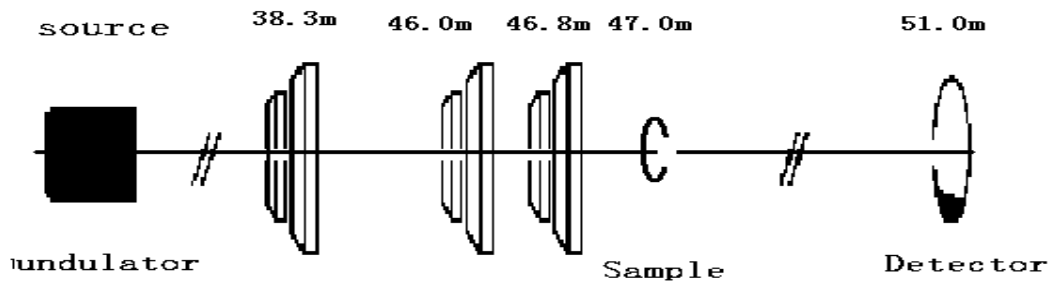
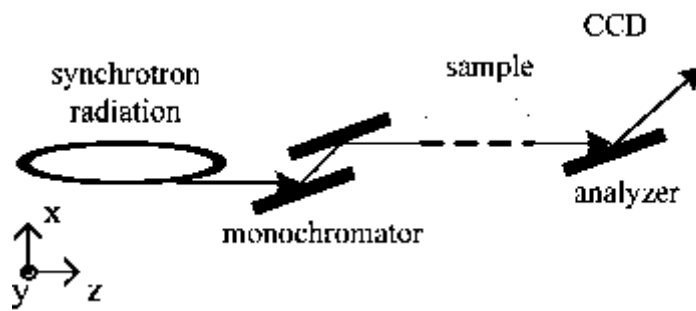**FIG. 5:** Layout of a X-ray coherent diffractive imaging system.

FIG. 6: Schematic layout of a X-ray diffraction enhanced imaging system.
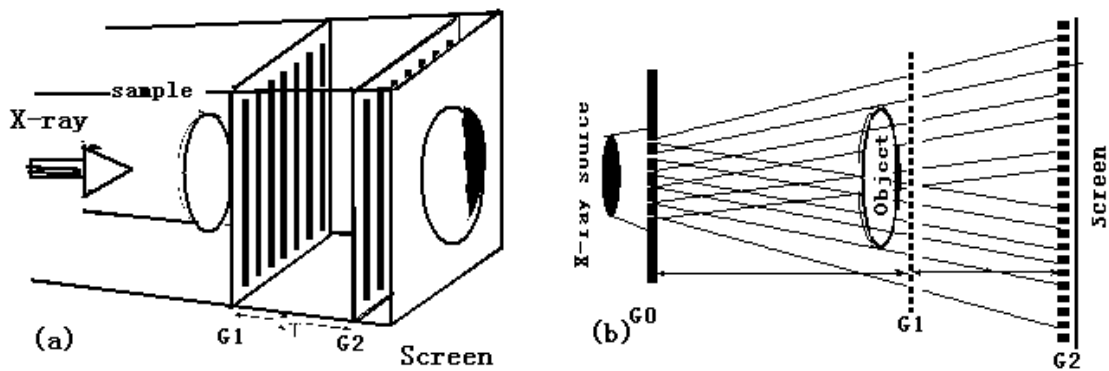

FIG. 7: Simplified layout of (a) X-ray Talbot interferometry and (b) a Talbot‑Lau interferometer.
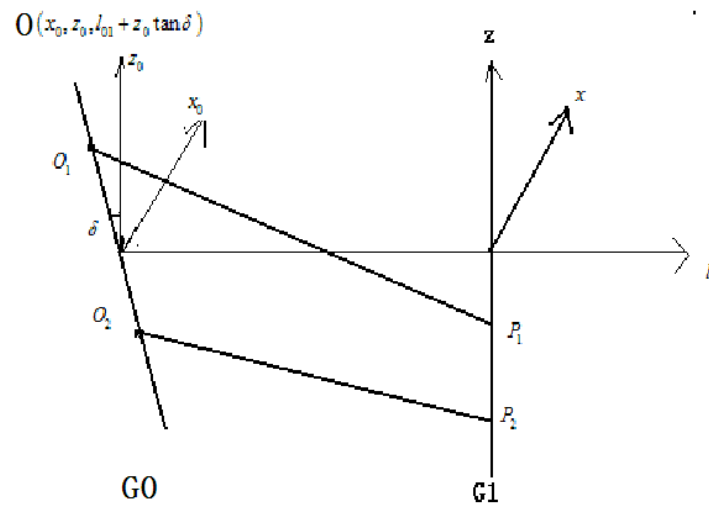
Fig. 8 The planes of the grating G0 and grating G1

Table 1: DAΦNE electron beam emittances and source sizes.

	E=0.5 GeV	E=0.7 GeV
$\sum_x$ [m rad]	10^{-6}	10^{-7}
$\sum_z$ [m rad]	10^{-8}	10^{-9}
$\int_x$ [mm]	4.13	1.3
$\int_z$ [mm]	0.109	0.035

Table 2: Parameters of the imaginary source.

Imaginary source	$\sigma_x (cm)$	$\sigma_z (cm)$	$\sigma'_x (mrad)$	$\sigma'_z (mrad)$	Flux 5 mrad (H) 1 eV bw (photons)
	0.79	0.015	2.13	0.36	2.18 e13

Table 3: Parameters of the secondary source.

Secondary source		Position	Image size $FWHM_{x_s} \times FWHM_{z_s}$ (cm)	Angle of the divergence $\sigma'_{x_s} \times \sigma'_{z_s}$ (mrad)	Flux (photons/sec/1A)
HFM& VFM setup	horizontal	entrance slit	1.77	4.88	1.37 e12
	vertical	exit slit	0.009	0.36	
Dragon-like system	horizontal	0.624 m before entrance slit	0.617	2.60	1.88 e12
	vertical	exit slit	0.03	1.21	

Table 4: Parameters of the grating 1

		Image size (cm) $FWHM_x \times FWHM_z$	Coherence width $\sigma_{\Delta x} \times \sigma_{\Delta z} \left(\mu m \times \mu m \right)$	Curve radius (vertical) R_{v1}
0 plane (exit slit)	HFM& VFM setup	10.4*0.009	0.1930*0.4421	∞
	Dragon-like system	3.9*0.03	0.1641*0.1327	∞
G1 plane (2 m from 0 plane)	HFM& VFM setup	12.74*0.194	0.2347*8.323	2.0057
	Dragon-like system	5.0549*0.5648	0.2134*2.4970	2.0057

Table 5: Parameters of the Talbot interferometer

Grating line: horizontal						
Monochromator		Position (from 0 plane)	Period (μm)	Source size H*V (cm)	Fourier coefficient	Pixel size (μm)
HFM& VFM system	G1	2 m	5.00	12.74 *0.194	/	/
	G2	38.2 mm	5.10	12.78* 0.197	$c_1 / \sqrt{c_0} = 0.48$	/
	Detector	38.2 mm	/	/	/	25
Dragon-like system	G1	2 m	5.00	5.0549* 0.5648	/	/
	G2	12.6 mm	5.03	5.0614 0.5684	$c_1 / \sqrt{c_0} = 0.48$	/
	Detector	12.6 mm	/	/	/	25

Table 6: Parameters of the Talbot-Lau interferometer

Grating line: horizontal									
Dragon-like system	**HFM&VFM system**	**Source slit or multi-slits**		**Grating G1**		**Grating G2**		**Detector**	
Position: (from vertical secondary source)		0 m		2 m		2 m + 480.62 mm		2 m + 480.62 mm	
Opening size (μm)		10.30							
Period (μm)		25.80		5		6.2		/	
Source size (cm) (H*V)		$FWHM_{x_0} \times FWHM_{z_0}$		$W_{x_1} \times W_{z_1}$		$W_{x_2} \times W_{z_2}$		$W_{x_2} \times W_{z_2}$	
		3.9*0.03	10.4*0.009	5.0549*0.5948	12.74 0.203	5.3392*0.7304	13.284*0.2188	5.3392*0.7304	13.284*0.2496
Coherence width (μm)		$\sigma_{\Delta x_0} \times \sigma_{\Delta z_0}$		$\sigma_{\Delta x_1} \times \sigma_{\Delta z_1}$		/		/	
		0.1641*0.1327	0.1930*0.4421	0.2134*77.5	0.2347*77.5				
Fourier coefficient		/		l=0, (1+i)/2 l=±odd, (1-i)/(iπl)		$c_1 / \sqrt{c_0} = 0.48$		/	
Pixel size (μm)		/		/		/		25	

Table 7: Comparisons among performances of a Talbot and a Talbot-Lau interferometer.

HFM&VFM system	Dragon-like system	Talbot interferometer		Talbot-Lau interferometer	
Number of scans (H*V)		1 * 26	1*9	1* 25	1*9
Photons x pixel (/25 μm)		7.3×10^7	7.9×10^8	1.2×10^6	1.2×10^6
Dose (Gy)		405	4357	6.8	6.9
Total time (s)		551	1727	23	7
Resolution (H*V) (μm)		24 * 25	24 * 25	24 * 20	24*20

Table 8 Stability of the source

Imaginary source	Monochromator (*μrad*)	Talbot-Lau interferometry (*mrad*)
HFM&VFM	3.44 (V)	6.37(H)*0.085(V)
Dragon-like system	7.72 (V)	2.53(H)*0.282(V)